OPEN ACCESS

ARTICLE

The Innovation Neurology

A parallel-serial DNA nanodevice enables multichannel decoding of the BACE1-AS1/BACE1 axis in Alzheimer's disease

Tao Cheng,[1] Jiabao Yu,[1] Heng Zhou,[1] Jiaying Sun,[1] Zheng Xu,[1] Jianwei Jiao,[1,*] and Jin Jiao[1,*]

*Correspondence: jwjiao@ioz.ac.cn (J.J); jiaojin@sdfmu.edu.cn (J.J.)

Received: ; Accepted: July 17, 2026; https://doi.org/10.59717/j.tine.2026.100005

GRAPHICAL ABSTRACT

ARTICLE

OPEN ACCESS

A parallel-serial DNA nanodevice enables multichannel decoding of the BACE1-AS1/BACE1 axis in Alzheimer's disease

Tao Cheng,[1] Jiabao Yu,[1] Heng Zhou,[1] Jiaying Sun,[1] Zheng Xu,[1] Jianwei Jiao,[1,*] and Jin Jiao[1,*]

[1]Shandong Cancer Hospital and Institute, Shandong First Medical University and Shandong Academy of Medical Sciences, Jinan 250117, China

[2]State Key Laboratory of Stem Cell and Reproductive Biology, Institute of Zoology, Chinese Academy of Sciences, Beijing 100101, China

*Correspondence: jwjiao@ioz.ac.cn (J.J); jiaojin@sdfmu.edu.cn (J.J.)

Received: ; Accepted: July 17, 2026; https://doi.org/10.59717/j.tine.2026.100005

Citation: Cheng T., Yu J., Zhou H., et al. (2026). A parallel-serial DNA nanodevice enables multichannel decoding of the BACE1-AS1/BACE1 axis in Alzheimer's disease. *The Innovation Neurology* **1**:100005.

The accurate decoding of molecular interactions within disease related signaling pathways remains a central challenge for early and reliable diagnosis of Alzheimer's disease (AD). While individual biomarkers such as BACE1 and its antisense transcript BACE1-AS1 have been widely studied, their coupled behavior within a functional axis is difficult to interpret using single output biosensing schemes. Here, we report a parallel–serial DNA nanodevice that translates the joint activity of the BACE1-AS1/BACE1 axis into structured, multichannel fluorescence outputs. Built around a hexagram DNA scaffold, the nanodevice undergoes distinct cleavage patterns in response to BACE1, BACE1-AS1, or their coexistence, which are subsequently converted into programmable downstream logic operations. Unlike conventional AND or OR logic gates that produce a single binary signal, this design combines parallel recognition with serial validation, generating three coordinated fluorescence readouts that reflect different states of pathway activity. By integrating the multichannel outputs with machine learning (ML) models, AD samples can be validated. Feature attribution analysis further reveals that BACE1-AS1 contributes more strongly than BACE1 to the diagnostic decision. By coupling DNA logic with multichannel signal cooperation, this work provides a practical route for translating molecular inputs into pathway level descriptions and clinically interpretable outcomes in AD.

INTRODUCTION

Alzheimer's disease (AD) is a progressive neurodegenerative disorder characterized by memory loss, cognitive impairment, and synaptic dysfunction.[1-4] With the rapid aging of the global population, its social and economic burden continues to increase. Despite extensive efforts, early and reliable diagnosis of AD remains difficult, as pathological changes often precede clinical symptoms by many years.[5-9] This temporal gap between molecular pathology and clinical manifestation highlights the need for analytical approaches that can sensitively probe disease related molecular processes while offering interpretable biological insight.

Among the molecular events implicated in AD, the β-site amyloid precursor protein cleaving enzyme 1 (BACE1) and its antisense transcript BACE1-AS1 have attracted increasing attention.[10-12] BACE1 is a key enzyme involved in amyloid-β production, while BACE1-AS1 stabilizes BACE1 mRNA through antisense pairing and protection from nucleolytic degradation.[13] Rather than acting independently, these two components form a coupled regulatory axis whose dysregulation is closely associated with early disease development. As a result, the joint behavior of BACE1 and BACE1-AS1 carries richer information than either marker alone.

However, interpreting the activity of such a two-component axis remains challenging. Most existing biosensing strategies focus on single target detection or rely on simple binary logic operations, such as AND or OR gates, which produce only one output signal and are insufficient to describe coordinated or intermediate states within disease related signaling axes.[14-18] In addition, amplification schemes directly triggered by target binding, including hybridization chain reaction (HCR) and catalytic hairpin assembly (CHA), may suffer from background leakage in complex biological environments, compromising signal reliability and interpretability.[19-21] These limitations make it difficult to extract structured information about pathway coordination from molecular readouts alone.

Recent studies have shown that multichannel molecular signals, when analyzed collectively, can provide a more informative description of disease states, and machine learning offers a practical means to integrate such features for classification and interpretation[22-28]. Here, we construct a parallel–serial DNA nanodevice (PSDN) that translates the coupled activity of the BACE1-AS1/BACE1 axis into coordinated multichannel fluorescence outputs. The design is built around a hexagram DNA scaffold that responds differently to BACE1, BACE1-AS1, or their coexistence, producing distinct cleavage patterns that trigger downstream logic operations. By combining parallel target recognition with serial signal validation, the nanodevice generates structured fluorescence signals that reflect different states of pathway activity. When applied to clinical samples, these multichannel outputs support both disease classification and pathway state description, and integration with machine learning analysis enables robust discrimination between AD patients and healthy controls while clarifying the relative contribution of BACE1-AS1 and BACE1.

EXPERIMENTAL SECTION

Instruments

The fluorescence emission spectra of FAM, TAMRA, and Cy5 dyes were measured using a multifunctional microplate reader (Spark Tecan, Switzerland), with excitation wavelengths of 462 nm, 530 nm, and 615 nm, respectively. All reactions were performed in a black 384-well plate. Gel images were carried out on a ChemiScope 6200 (Clinx Science Instruments, China), and nucleic acids mixtures were prepared using an HC-100 thermocoupling mixer (Thermo Fisher Scientific, China).

Materials and reagents

The buffers used in this study were as follows: TM buffer (0.5 M Tris-HCl, 80 mM MgSO4, pH 7.5); TE buffer (10 mM Tris-HCl, 1 mM EDTA, pH 8.0); and 1 × TEB (89 mM Tris-HCl, 2 mM EDTA, pH 8.0). Other reagents, including GelRed and 30% acryl/bis solution (19:1) were purchased from Sangon Biotechnology. Human serum samples were supplied by Jinan Central Hospital (China). The study was approved by the Medical Ethics Committee of Shandong First Medical University (approval No.: R202111230199). The oligonucleotide sequences were HPLC-purified and synthesized by Shanghai Sangon Biotechnology Co., Ltd., (Shanghai, China). The sequences of the oligonucleotides were listed in Table S1.

Agarose gel electrophoresis (AGE)

A 2% agarose gel was prepared by adding 1 g of agarose powder into 49 mL of 1 × TBE buffer. The mixture was heated to a boil with continuous stirring until the solution turned completely clear. Electrophoresis was performed in 1 × TBE running buffer at 120 V for 60 min, after which the gel was scanned using a ChemiScope 6200 system.

Polyacrylamide gel electrophoresis (PAGE)

10% PAGE was performed using 1 × TBE buffer. Loading samples were prepared by mixing 10 μL of nucleic acid samples, 1 μL of Gel Red, and 2 μL of 6 × DNA loading buffer. Electrophoresis was conducted at 100 V for 45 min, after which the gel was scanned with a ChemiScope 6200 imaging system.

Sensitivity investigation

For dual-target sensitivity testing, 250 nM PSDN was incubated with differ-

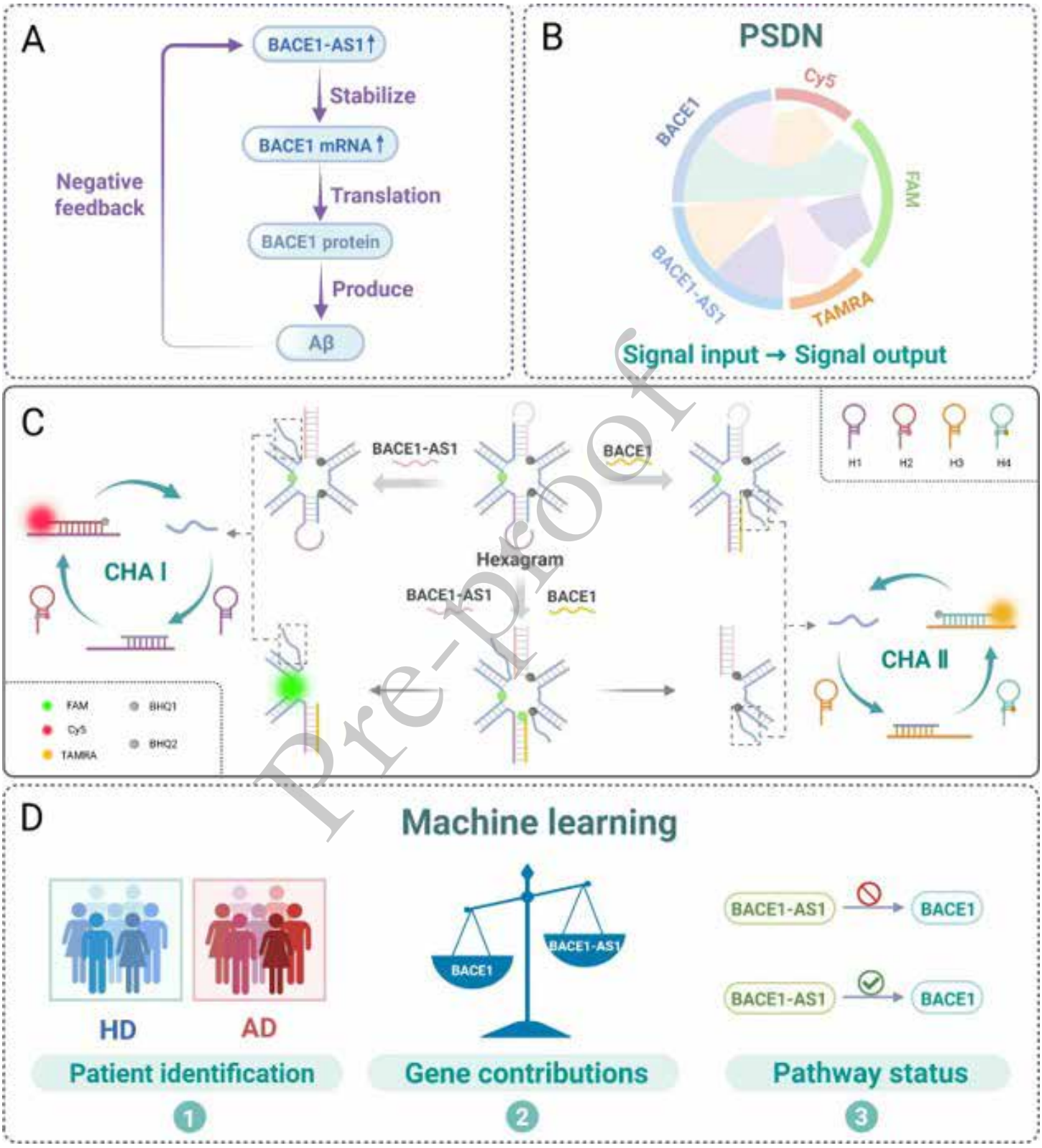

Scheme 1. Schematic illustration of machine learning-enhanced parallel-serial DNA nanodevice (PSDN) for multidimensional dissection of the BACE-AS1/BACE1 axis.

ent concentrations of BACE1 (0, 0.1, 0.5, 1, 2, 5, 10, 25, 50, 100, 250 nM) in the presence of BACE1-AS1 (250 nM). 250 nM PSDN was incubated with BACE1-AS1 at different concentrations (0, 0.1, 0.5, 1, 2, 5, 10, 25, 50, 100, 250 nM) in the presence of BACE1 (250 nM). All samples were reacted at 37°C for 60 min, and their fluorescence spectra were recorded with an excitation wavelength of 462 nm and an emission range of 504–600 nm. For single-target sensitivity testing, 250 nM PSDN was incubated with different concentrations of BACE1 (0, 0.01, 0.1, 1, 10, 20, 50, 100, 250 nM) or BACE1-AS1 (0, 0.01, 0.1, 1, 10, 20, 50, 100, 250 nM). All samples were maintained at 37°C for 60 min. Fluorescence spectra were acquired with two sets of parameters: 530 nm (excitation) and 570–670 nm (emission), as well as 615 nm (excitation) and 650–750 nm (emission).

Specificity assay

For dual-target specificity testing, 250 nM PSDN was incubated with 250 nM BACE1 and 250 nM BACE1-AS1, or combinations of BACE1, BACE1-

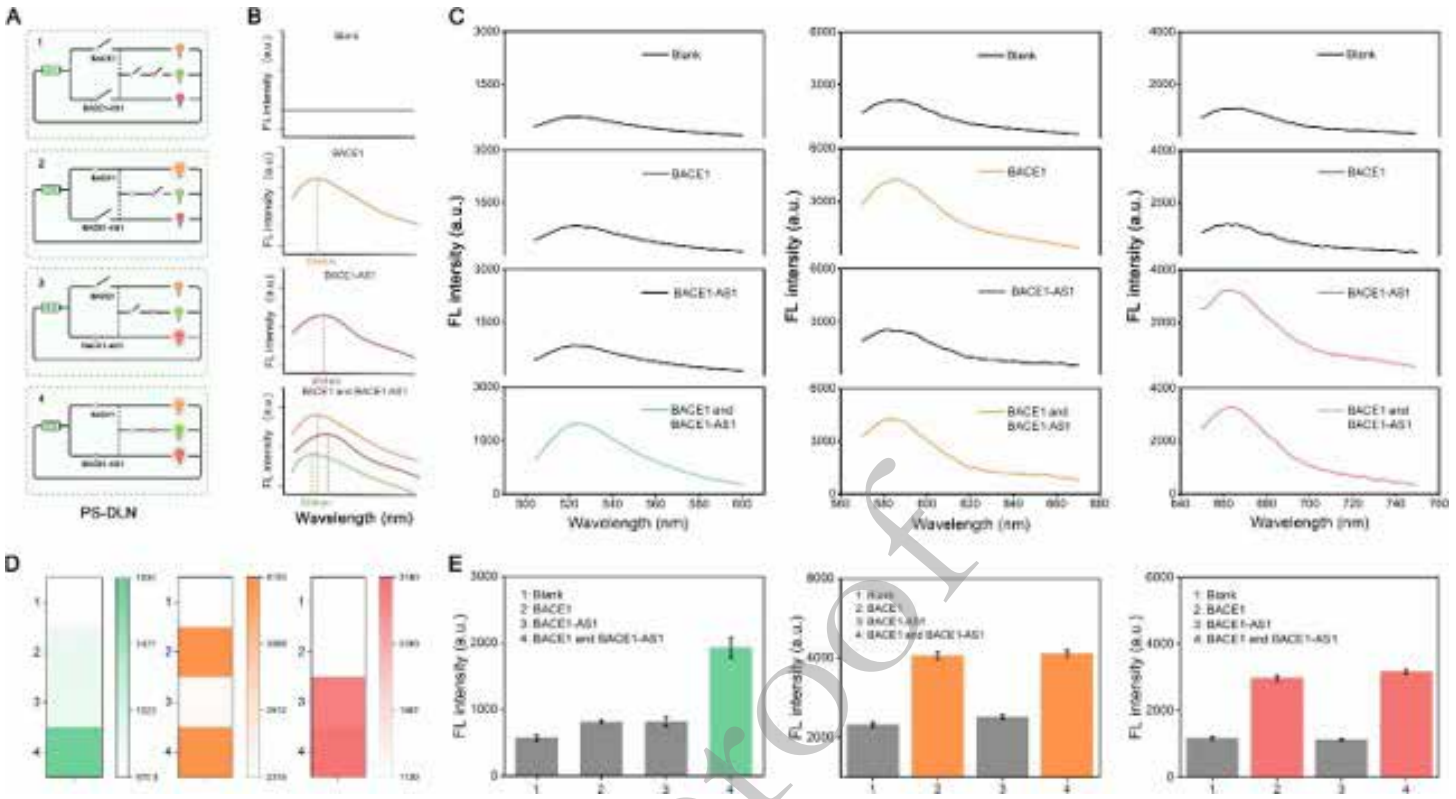

Figure 1. (A) Schematic diagram of the PSDN system with BACE1 and BACE1 switches. (B) Graphical depiction of fluorescence responses to different inputs. (C) Fluorescence spectra analysis and (D) Heatmap of different inputs (Blank, BACE1, BACE1-AS1, BACE1 and BACE1-AS1) in three fluorescence channels: FAM (left), TAMRA (middle), and Cy5 (right). (E) Peak responses for the Blank, BACE1, BACE1-AS1, BACE1 and BACE1-AS1 in the three fluorescence channels (BACE1 concentration: 250 nM; BACE1-AS1 concentration: 250 nM). Error bars, SD, *n*=3.

AS1 with other genes (miR-21, miR-221, miR-155, miR-193b). All samples were reacted at 37°C for 60 min, and their fluorescence spectra were recorded with an excitation wavelength of 462 nm and an emission range of 504–600 nm. For single-target specificity testing, 250 nM PSDN was incubated with 250 nM BACE1 or 250 nM BACE1-AS1, along with other parallel miRNAs (miR-21, miR-221, miR-155, and miR-193b). All samples incubated at 37°C for 60 min. Fluorescence spectra were recorded with two sets of parameters: excitation wavelength of 530 nm (emission range: 570–670 nm) and excitation wavelength of 615 nm (emission range: 650–750 nm).

Statistical analysis

Statistical analyses were performed with GraphPad Prism 9.0 software. Data are presented as mean ± standard deviation (SD) from at least three independent experiments ($n \geq 3$). Differences between groups were evaluated by two-tailed Student's *t*-test. Statistical significance was defined as $*p < 0.05$, $**p < 0.01$, $***p < 0.001$, $****p < 0.0001$.

Machine learning model construction

Ten classical ML algorithms were selected to classify healthy subjects and AD patients, spanning categories including KNN, ElasticNet, Naive Bayes, Partial Least Squares Regression (PLS), Bayesian Generalized Linear Model (Bayesian GLM), Decision Tree (C5.0), Neural Network, Random Forest, Extreme Gradient Boosting (XGBoost), and Multivariate Adaptive Regression Splines (MARS). All models were implemented in RStudio. Ten-fold cross-validation (with three repetitions) was employed, using areas under the curve (AUC) as the core metric to optimize model performance and ensure discriminative ability in classification.

Model performance evaluation

Accuracy, sensitivity, and specificity were calculated from the confusion matrix: Sensitivity reflects the model's ability to identify AD patients, while specificity denotes its ability to distinguish the control group. The Youden index (J = sensitivity + specificity - 1) was used to determine the optimal classification threshold, with its maximum value corresponding to the optimal cutoff point that balances sensitivity and specificity.

Visual analysis

AUC histograms were plotted for various ML models to illustrate differences in classification efficacy among algorithms. Additionally, receiver operating characteristic (ROC) curve comparisons were constructed between single fluorescence channel indicators and the optimal ML model. For top-performing models, confusion matrix heatmaps were generated to visualize classification outcomes. Furthermore, SHAP analysis was employed to quantify each feature's contribution to the model's predictive outcomes, thereby revealing key biomarkers that drove model decisions.

RESULTS AND DISCUSSION

Working mechanism and feasibility of the PSDN

The PSDN is designed to respond to the coupled activity of the BACE1-AS1/BACE1 axis through a combination of target recognition and downstream signal transduction. As shown in Scheme 1, a hexagram DNA scaffold is assembled as the responsive unit, incorporating two recognition elements corresponding to BACE1 and BACE1-AS1. This design allows the nanodevice to distinguish between the presence of either target alone and their coexistence. When exposed to BACE1 or BACE1-AS1 individually, the hexagram scaffold undergoes partial cleavage. In contrast, the simultaneous presence of both targets leads to a more extensive cleavage of the scaffold. These different cleavage states reflect distinct molecular input conditions of the BACE1-AS1/BACE1 axis. The resulting cleavage products subsequently initiate CHA reactions, converting structural changes of the scaffold into fluorescence signals. The signal generation process follows a parallel–serial logic pattern. Recognition of BACE1 and BACE1-AS1 occurs in parallel at the scaffold level, whereas downstream signal propagation proceeds in a serial manner, depending on the specific cleavage pattern. As a result, three fluorescence channels are activated in different combinations under single-target and dual-target conditions. Compared with conventional binary logic gates that yield a single output, this design provides multiple readouts corresponding to different molecular input states.

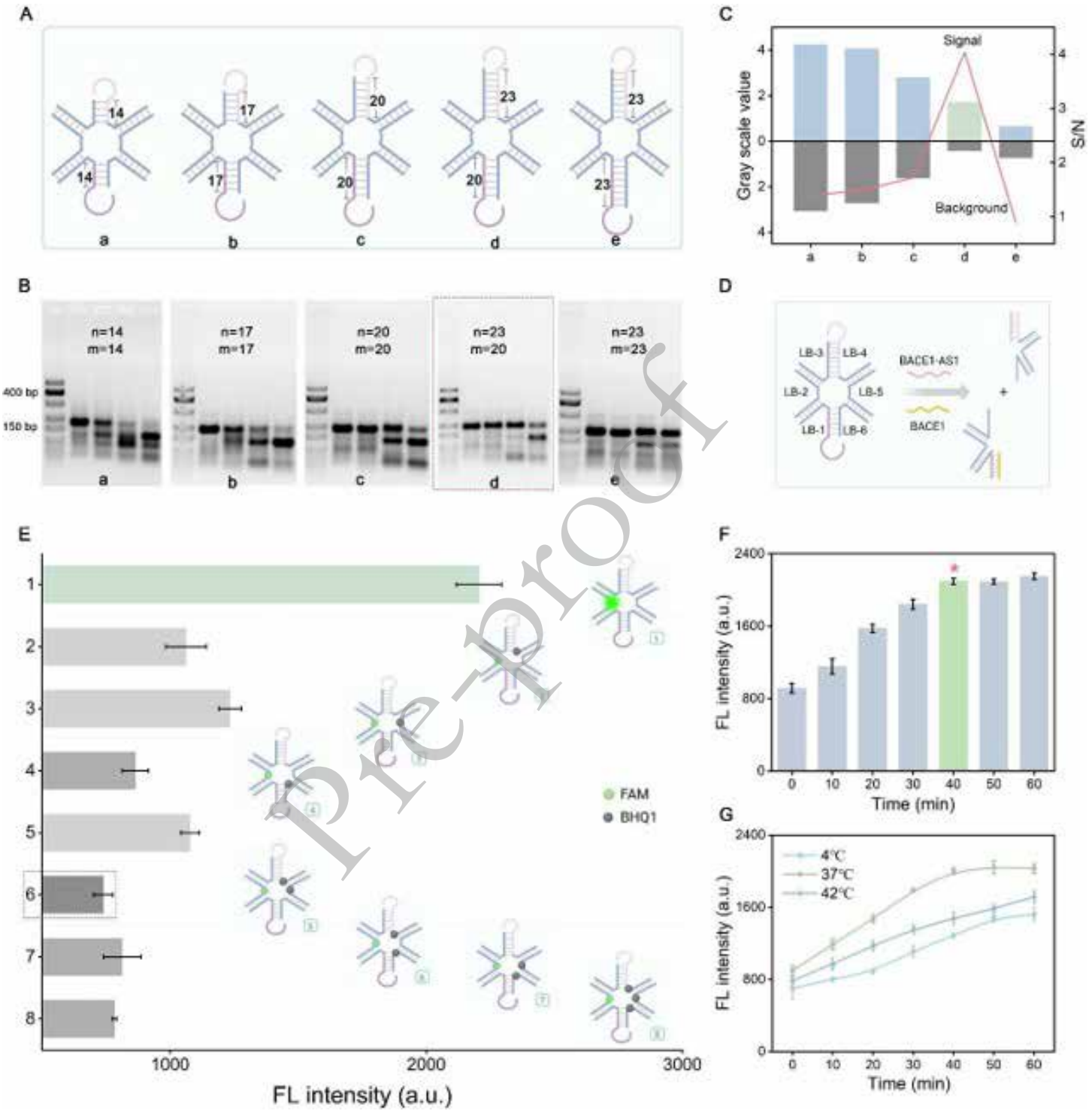

Figure 2. (A) Schematic diagram of hexagram with different stem lengths. (B) Agarose gel for different inputs (a-e: lane 1: marker; lane 2: hexagram; lane 3: hexagram + BACE1; lane 4: hexagram + BACE1-AS1; lane 5: hexagram + BACE1 and BACE1-AS1). (C) Gel band quantification: new bands (separate BACE1-AS1/BACE1 = Background; co-addition = Signal). (D) Schematic diagram of the complete cleavage of the hexagram in the presence of BACE1 and BACE1-AS1. (E) Fluorescence of BHQ1-mediated FAM quenching at different positions. (F) Optimization reaction time of the proposed PSDN biosensor. (G) Optimization reaction temperature of the proposed PSDN biosensor. Error bars, SD, *n*=3.

The feasibility of the nanodevice is examined by gel electrophoresis and fluorescence measurements. AGE shows a gradual decrease in electrophoretic mobility with the stepwise assembly of the hexagram scaffold, confirming its successful formation (Figure S1). Fluorescence measurements indicate that BACE1 selectively induces the TAMRA signal, while BACE1-AS1 preferentially activates the Cy5 channel. When both targets are present, FAM, TAMRA, and Cy5 signals are simultaneously observed (Figure 1A-B), consistent with the expected logic operation (Figure S2). Figure 1C summarizes the fluorescence responses under blank, single-target, and dual-target conditions. The FAM channel responds specifically to the coexistence of BACE1 and BACE1-AS1, whereas the TAMRA and Cy5 channels respond to the individual targets as well as to their combination (Figure 1D-E). Time-dependent fluorescence measurements show a gradual increase in signal intensity following target addition, reaching a stable level within approximately 40 min (Figure S3-5), which is consistent with the kinetics of the amplification reactions involved.

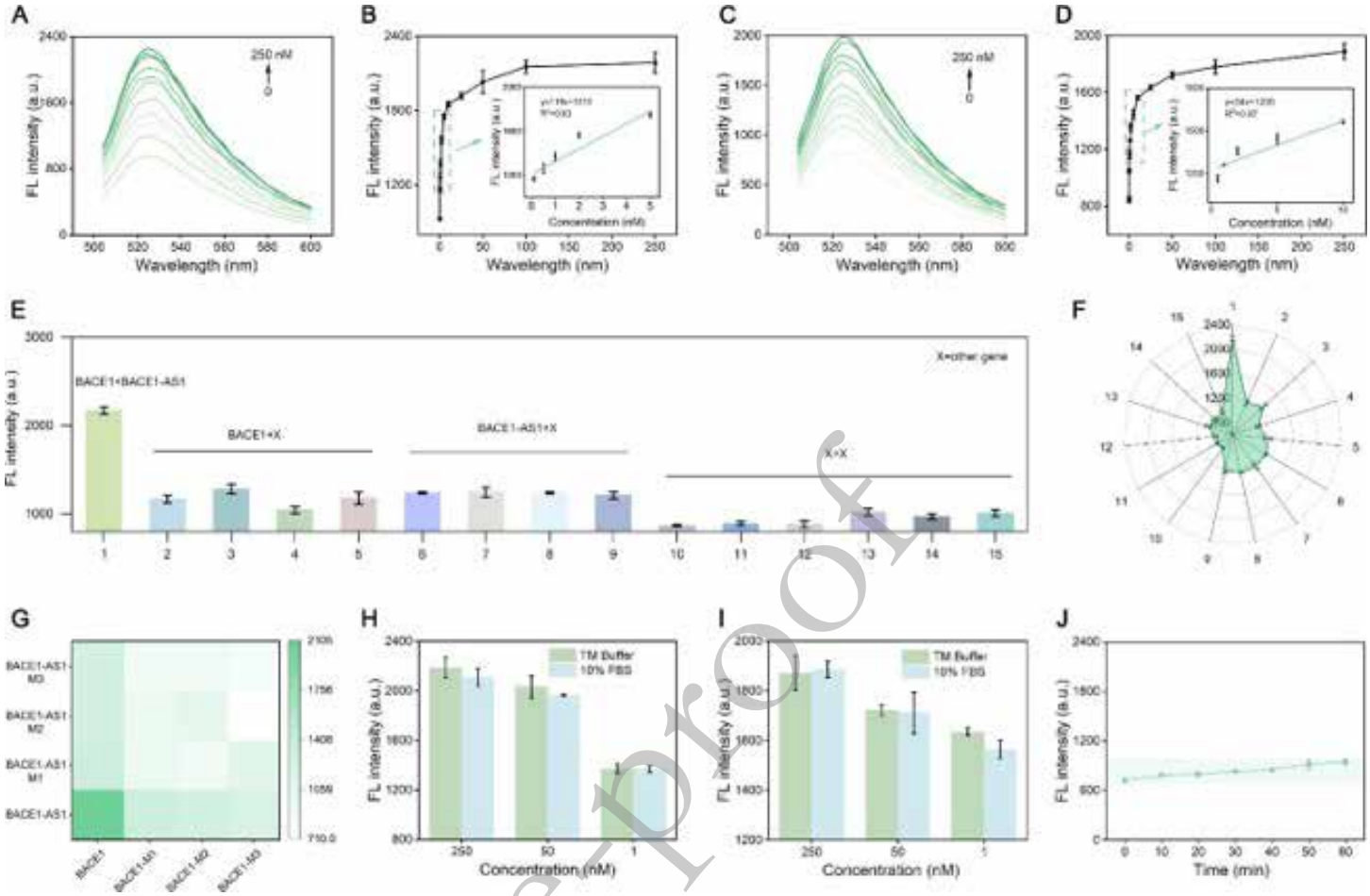

Figure 3. (A) Fluorescence curves for BACE1 at different concentrations (0, 0.1, 0.5, 1, 2, 5, 10, 25, 50, 100, 250 nM) with BACE1-AS1 maintained at 250 nM. (B) The linear relationship between fluorescence response and BACE1 concentration. (C) Fluorescence curves for BACE1-AS1 at different concentrations (0, 0.1, 0.5, 1, 2, 5, 10, 25, 50, 100, 250 nM) with BACE1 fixed at 250 nM. (D) The linear relationship of fluorescence response with BACE1-AS1 concentration. (E) Column charts and (F) Radar charts show selective fluorescence responses of BACE1 and BACE1-AS1, and other co-existing combinations: 2) BACE1 + miR-21; 3) BACE1 + miR-221; 4) BACE1 + miR-155; 5) BACE1 + miR-193b; 6) BACE1-AS1 + miR-21; 7) BACE1-AS1 + miR-221; 8) BACE1-AS1 + miR-155; 9) BACE1-AS1 + miR-193b; 10) miR-21 + miR-221; 11) miR-21 + miR-155; 12) miR-21 + miR-193b; 13) miR-221 + miR- 155; 14) miR-221 + miR-193b; 15) miR-155 + miR-193b (all at 250 nM). (G) The selectivity response of fluorescence toward BACE1 and BACE1-AS1, and various other mismatched RNAs (all at 250 nM). (H) Fluorescence intensities in TM buffer and 10% FBS with varying BACE1 concentrations. (I) Fluorescence intensities in TM buffer and 10% FBS with varying BACE1-AS1 concentrations. (J) Capability of the PSDN to avoid false-positive signals (FAM channel). Error bars, SD, *n*=3.

These results indicate that the PSDN nanodevice produces distinct multichannel fluorescence responses under different input conditions. This behavior supports its use in subsequent quantitative analysis of the BACE1-AS1/BACE1 axis.

Optimization of experimental parameters

To obtain stable and reproducible signal outputs, experimental parameters influencing the structural behavior of the PSDN were examined. The optimization focused on the hexagram scaffold and the reaction conditions required for consistent signal generation, while avoiding unnecessary complexity in device design. Firstly, we have designed five hexagrams with different stem lengths: a (n=14, m=14), b (n=17, m=17), c (n=20, m=20), d (n=23, m=20), and e (n=23, m=23) to optimize their assembly and disassembly under dual-target conditions (Figure 2A). The key to successful operation of the PSDN system requires no response to a single target and efficient disassembly in the presence of dual targets. We therefore have investigated this characteristic via AGE. Five sets of gel images (a–e) are obtained, where lanes 2 to 5 correspond to the hexagram alone, hexagram + BACE1, hexagram + BACE1-AS1, and hexagram + BACE1 and BACE1-AS1, respectively. Notably, no new lower molecular weight bands appear in the absence of targets (Gel a-e; lane 2), indicating that the hexagram maintains stable integrity. Adding BACE1, new lower molecular weight bands emerge, suggesting non-specific disassembly (Gel a and b, lane 3). Similarly, adding BACE1-AS1 alone leads to new lower molecular weight bands, also indicating leakage (Gel b and c; lane 4). When both BACE1 and BACE1-AS1 are added, no clear new lower molecular weight bands are observed, implying excessive stability of the hexagram (Gel e; lane 5). Thus, we have selected the hexagram with stem d (n=23, m=20) for subsequent experiments (Figure 2B). Grayscale analysis of the gel images was used to compare background cleavage and target-induced responses among the five designs. The background is defined as the sum of the ratios of newly formed bands in the lower regions of Lanes 3 and 4 to their respective upper bands. The signal refers to the ratio of newly formed bands in the lower region of Lane 5 to its corresponding upper band (Figure 2C). In the absence of targets, the hexagram structure remains intact. Neither BACE1 nor BACE1-AS1 alone disrupts its assembly, and only the coexistence of BACE1 and BACE1-AS1 induces the disassembly of the hexagram structure (Figure 2D).

The placement of the quencher molecule BHQ1 on the hexagram scaffold was further examined. Seven labeling configurations were tested to evaluate fluorescence quenching behavior (Figure 2E, S6-7). Differences in background fluorescence were observed among the configurations. Mode 6 showed relatively lower background signals and was therefore used in the following experiments. Reaction conditions were then evaluated using time dependent fluorescence measurements. Following target addition, fluorescence intensity increased gradually and reached a stable level after approximately 40 min (Figure 2F). Temperature-dependent measurements indicated that reactions performed at 37°C produced consistent signal responses (Figure 2G). These conditions were adopted for subsequent experiments.

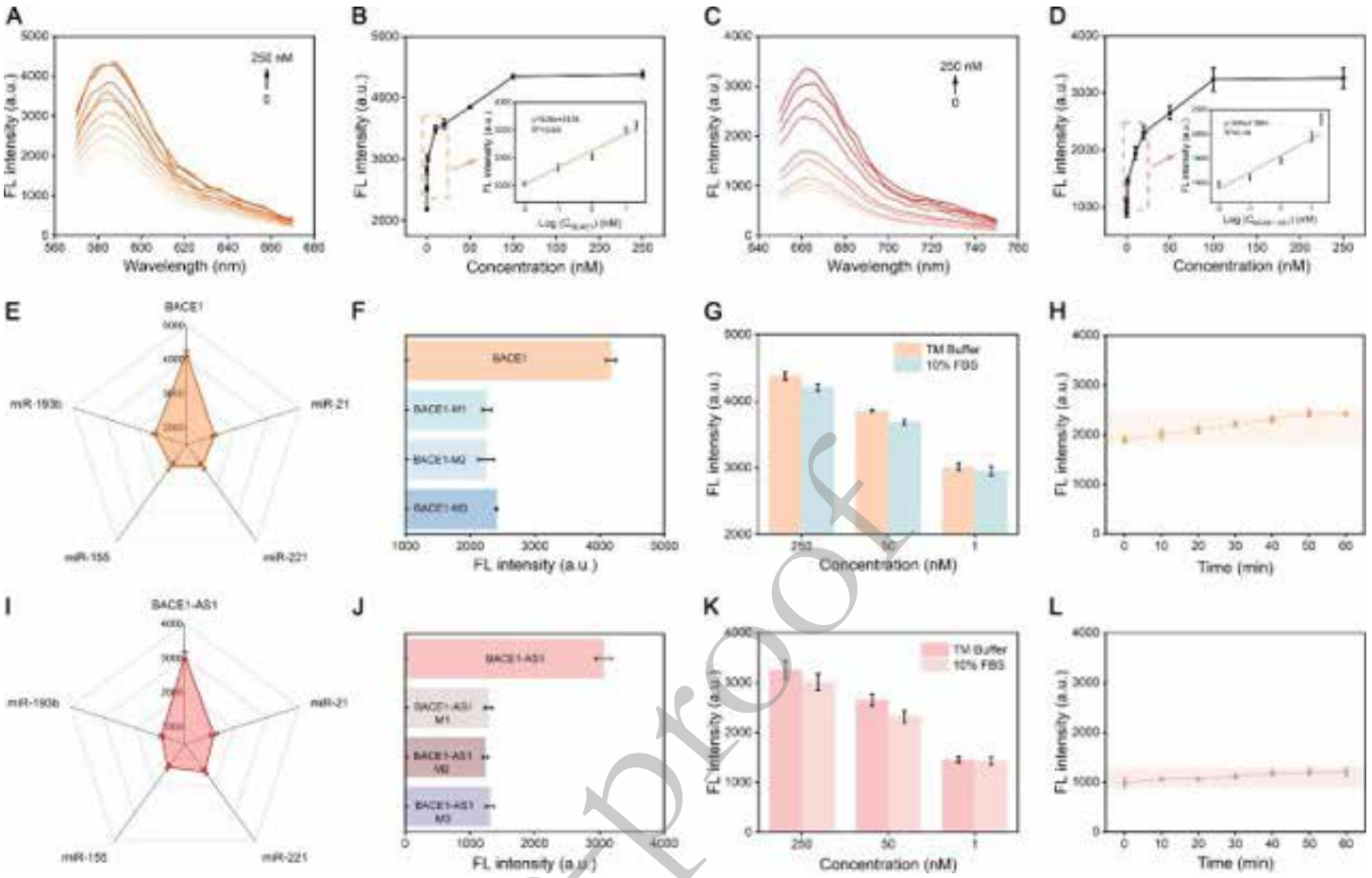

Figure 4. (A) Fluorescence curves of BACE1 at different concentrations (0, 0.01, 0.1, 1, 10, 20, 50, 100, 250 nM). (B) The linear relationship between fluorescence response and BACE1 concentration. (C) Fluorescence curves for BACE1-AS1 at different concentrations (0, 0.01, 0.1, 1, 10, 20, 50, 100, 250 nM) (D) The linear relationship of fluorescence response with BACE1-AS1 concentration. (E) Fluorescence selective responses of the system toward BACE1 and other interfering miRNAs (all at 250 nM). (F) Fluorescence selective responses of the system toward BACE1 and other mismatched mRNAs (all at 250 nM). (G) Fluorescence intensities of three concentrations of BACE1 measured in TM buffer and 10% FBS. (H) Ability of the PSDN to avoid false-positive signals (TAMRA channel). (I) Fluorescence selective responses of BACE1-AS1 and other interfering miRNAs (all at 250 nM). (J) Fluorescence selective responses of BACE1-AS1 and other mismatched LncRNAs (all at 250 nM). (K) Fluorescence intensities of three concentrations of BACE1-AS1 measured in TM buffer and 10% FBS. (L) Ability of the PSDN to avoid false-positive signals (Cy5 channel). Error bars, SD, *n*=3.

Finally, polyacrylamide gel electrophoresis was used to examine whether cleavage products derived from the hexagram scaffold could participate in downstream CHA reactions (Figure S8-9). The appearance of expected bands confirmed that the cleavage products were compatible with the designed signal transduction process under the selected conditions.

Dual-input performance

The analytical performance of the PSDN in the FAM channel is assessed under various concentrations of BACE1 (0-250 nM) and BACE1-AS1 (0-250 nM). As shown in Figure 3A, the fluorescence curve exhibits a gradually increasing peak signal with the elevation of BACE1 concentration (BACE1-AS1 fixed at 250 nM). The calibration curve reveals a detection range of 0.1-250 nM for BACE1 (Figure 3B). As shown in Figure 3C-D, similar results are observed for BACE1-AS1 (under the same concentration condition). The anti-interference ability is crucial for the biosensor. Accordingly, we select several small RNAs (miR-21, miR-221, miR-155, and miR-193b) as potential interferents to assess the sensor's specificity. A significant increase in fluorescence is observed in the presence of BACE1 and BACE1-AS1, whereas no significant difference is detected in the potential interferences (Figure 3E-F). Additionally, we design single-base, double-base, and three-base mutations (of BACE1 and BACE1-AS1) to investigate the PSDN's ability to recognize base mismatches. As shown in Figure 3G, fluorescence values are lower for sequence-mismatched samples compared to the BACE1 and BACE1-AS1 cases.

PSDN demonstrates good stability in 10% fetal bovine serum (FBS), with comparable fluorescence responses observed in TM buffer and diluted FBS (Figure 3H-I). Importantly, no significant fluorescence enhancement after 60 min without the target, demonstrating that the PSDN produces no false-positive signals (Figure 3J), confirming the low background of the system.

Single input performance

The multiple signal outputs may serve as a supplement to single signal outputs, thereby enhancing detection accuracy. Encouraged by the promising performance of the PSDN biosensor in the FAM fluorescence channel, we subsequently adopt CHA to achieve a high signal-to-noise ratio. The fluorescence curves in Figure 4A, 4C demonstrate that the TAMRA and Cy5 fluorescence peaks increase with increasing concentrations of BACE1 or BACE1-AS1. As shown in Figure 4B, 4D, the fluorescence signals exhibit a good linear correlation with the logarithms of BACE1 or BACE1-AS1 concentrations. The regression equations are y = 306x + 3129 or y = 345x + 1564, where y denotes peak fluorescence (TAMRA and Cy5) and x denotes the logarithmic concentrations of BACE1 or BACE1-AS1, respectively. The correlation coefficients (R^2) are 0.99 and 0.90. As calculated using the 3σ/k principle (where σ denotes the standard deviation of the background signal and k represents the slope of the calibration curve), the limits of detection (LODs) for BACE1 and BACE1-AS1 are 0.16 nM and 0.56 nM, respectively. This sensitivity is comparable to that of previously reported methods (Table S2).

High specificity is validated by introducing various miRNAs and mismatched sequences, which produced negligible fluorescence compared to perfectly matched targets (Figure 4E-F, 4I-J). Furthermore, the stability of PSDN is validated by testing various concentrations of BACE1 or BACE1-AS1 in 10% FBS (Figure 4G, 4K). Subsequently, we verify that PSDN does not generate false-positive signals in the TAMRA or Cy5 channels (Figure 4H, L). Recovery experiments in 10% FBS shows acceptable accuracy and precision

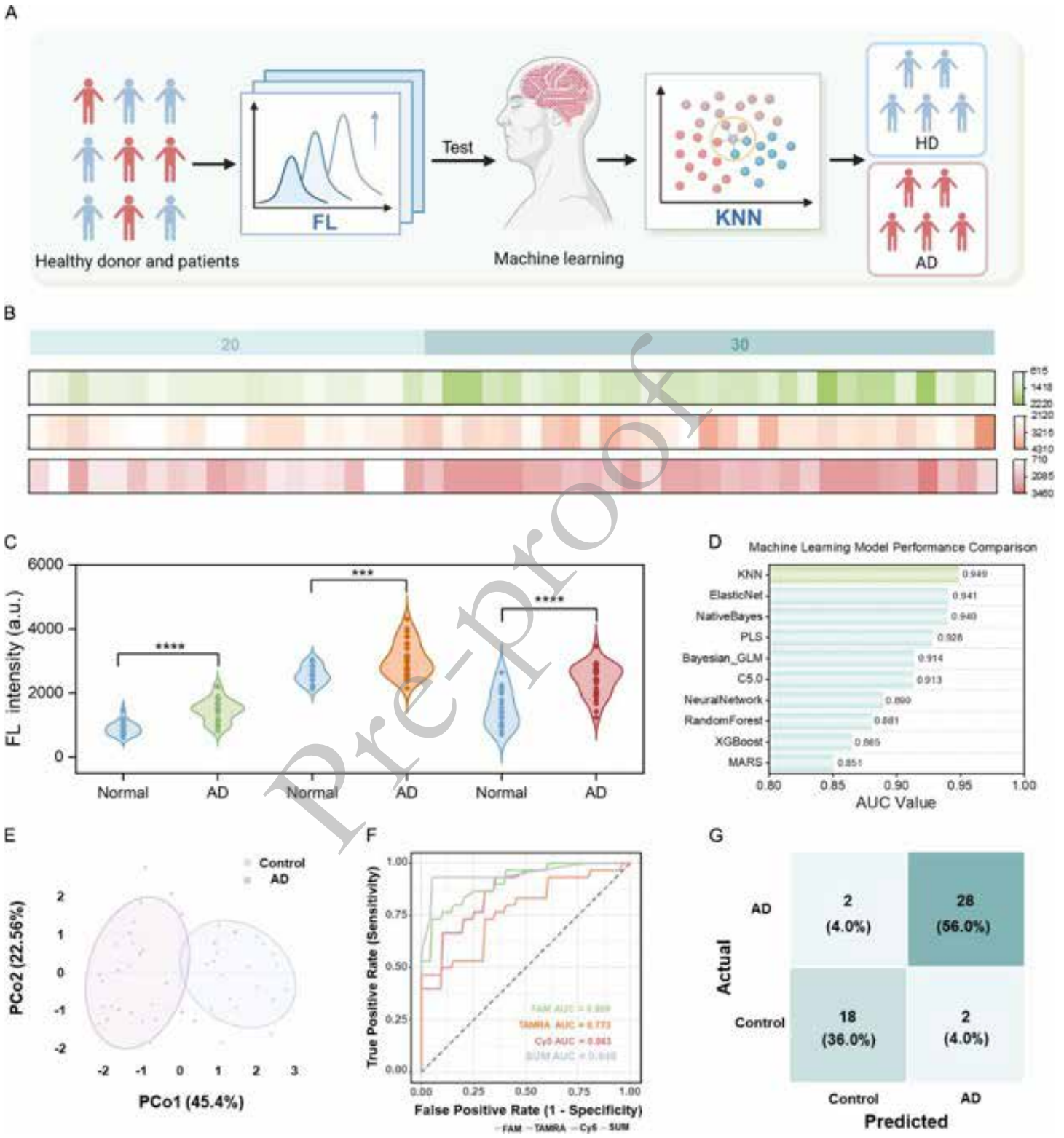

Figure 5. (A) Schematic of ML combined with the PSDN platform for differentiating healthy subjects from AD patients. (B) Fluorescence values measured through three channels by the PSDN in the clinical cohort are presented. (C) Violin plots of fluorescence intensities measured by the PSDN in healthy subjects among AD patients. (D) Areas under curve for ten distinct ML models are compared. AUC: area under the curve. (E) Principal Coordinates Analysis (PCoA) using the PSDN to distinguish healthy subjects from AD patients. (F) ROC analysis using the PSDN demonstrates the clinical diagnostic value of the platform in distinguishing between healthy subjects and AD patients. (G) Confusion matrix summarizing the discrimination performance of the method between healthy subjects and AD patients. *** $p < 0.01$, **** $p < 0.0001$. Error bars, SD, n=3.

(Table S3). These experimental results confirm that the proposed biosensing method exhibits excellent performance.

PSDN based clinical analysis in AD diagnosis

To evaluate the diagnostic applicability of PSDN, serum samples are collected from 20 healthy individuals and 30 AD patients (Table S4). As illustrated in Figure 5A, the PSDN assay combined with ML enables the discrimination between healthy subjects and AD patients. The three-channel fluorescence outputs clearly distinguished the two groups (Figure 5B-C, S10). As shown in Figure 5D, model performance is evaluated by comparing feature

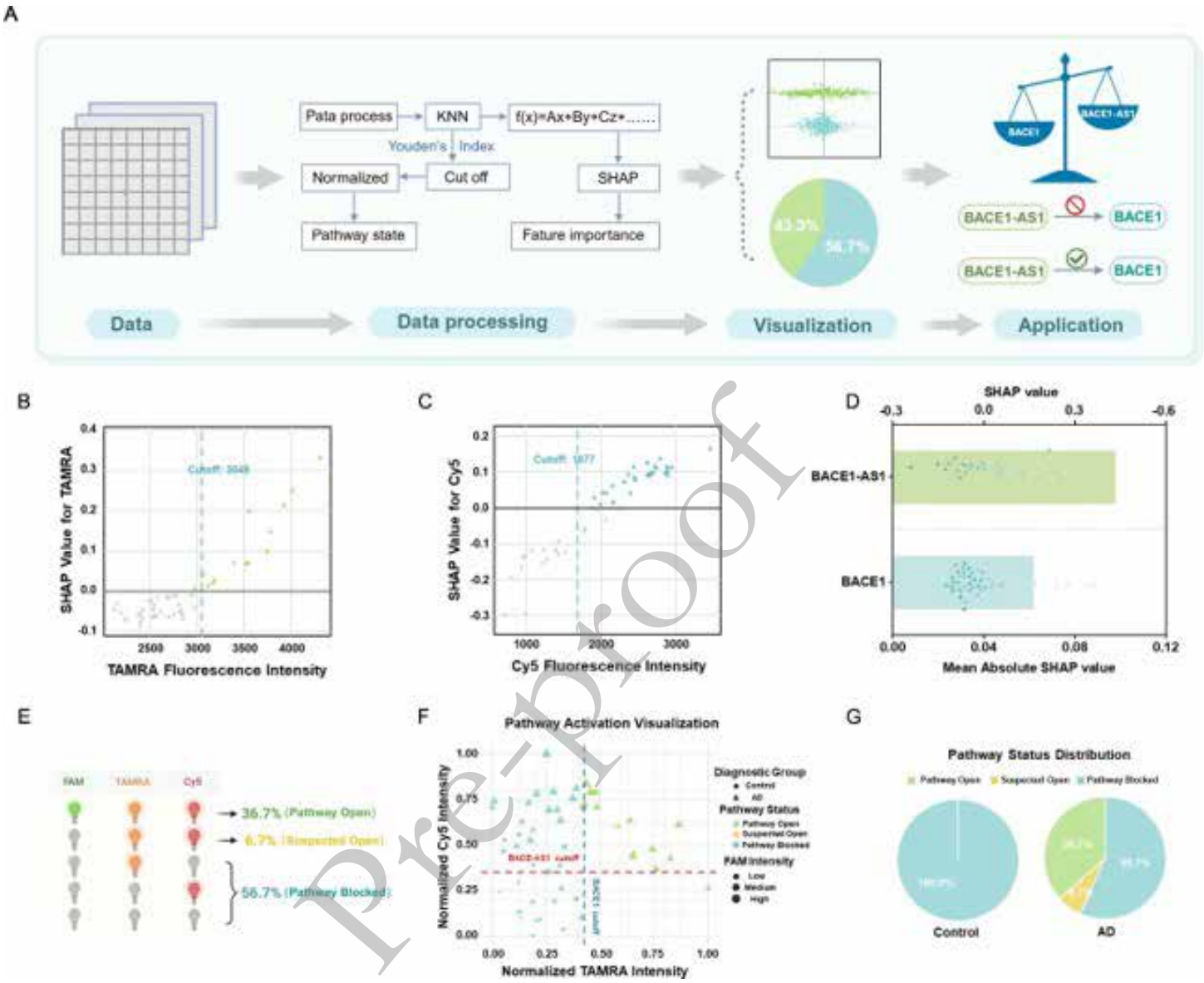

Figure 6. (A) Workflow for gene importance evaluation and pathway status assessment. (B) Scatter plot of BACE1 expression. (C) Scatter plot of BACE1-AS1 expression. (D) SHAP bee swarm plot. (E) Three channel fluorescence-based pathway status diagram. (F) Normalization of FAM, TAMRA, and Cy5 three-channel fluorescence signals enables visual pathway status analysis. (G) Pie chart presenting healthy subjects and AD sample status distribution.

sets. Data indicate the KNN model shows superior performance, so it is selected for subsequent analyses. Using fluorescence values, gender, and age as input variables for dimensionality reduction, we observe distinct clustering patterns between healthy subjects and AD patients (Figure 5E). Furthermore, analyzing data from the three fluorescence channels using ROC curves yield respective AUC of 0.909, 0.773, and 0.863, with a combined AUC of 0.949 (Figure 5F). As shown in Figure 5G, the KNN model confirms that the PSDN biosensor can readily distinguish between healthy subjects and AD patients. Additionally, the confusion matrix for diagnosing these groups shows a sensitivity of 90%, specificity of 93.3%, precision of 90%, and accuracy of 92% (Figure S11). These results highlight the strong diagnostic capability of PSDN when paired with ML.

Model explainability and pathway analysis

To understand the decision process of the ML models and connect it to biological relevance, SHAP analysis is performed (Figure 6A). The SHAP for attribution analysis on the model's predictions, quantitatively uncovering BACE1-AS1 and BACE1's contributions and influence directions in AD classification, and converting the model's "black box" decisions into feature importance rankings (Figure 6B-C). The SHAP importance score of BACE1-AS1 (0.0977) exceeds that of BACE1 (0.0617), indicating that BACE1-AS1 is a relatively more critical discriminative feature in the model's overall decision-making (Figure 6D). Subsequently, each fluorescent signals from three channel are normalized and subjected to thresholding, leading to the classification of real samples into states such as "pathway open", "suspected open", and "pathway blocked" (Figure 6E). "Pathway open" is defined as concurrent activation of FAM, TAMRA, and Cy5 fluorescence; "Suspected open" is classified as active TAMRA and Cy5 fluorescence with FAM inactive; and "pathway blocked" applies when only one of TAMRA or Cy5 is active, or both are inactive (Figure 6F). Among AD samples, Pathway open accounted for 36.7%, suspected open for 6.7%, and pathway blocked for 56.7% (Figure 6G, S12). This demonstrates that PSDN not only measures biomarker levels but also provides insight into pathway integrity at the clinical level.

CONCLUSION

In summary, we develop a PSDN biosensor integrated with ML for the analysis of the BACE1-AS1/BACE1 axis in AD. The system enables the discrimination of healthy subjects from AD patients while providing insight into the relative contributions of BACE1 and BACE1-AS1 through coordinated fluorescence readouts. The PSDN is designed to perform DNA logic operations on BACE1 and BACE1-AS1 inputs, generating multiple fluorescence responses that reduce ambiguity arising from single-signal measurements.

When combined with the KNN algorithm, the PSDN distinguishes healthy subjects from AD patients with a sensitivity of 90%, specificity of 93.3%, precision of 90%, and accuracy of 92%. Beyond group discrimination, the PSDN platform allows evaluation of the roles of BACE1 and BACE1-AS1 in clinical serum samples and provides information on the activity state of the BACE1-AS1/BACE1 axis. By organizing molecular inputs into interpretable multichannel signals and analyzing them collectively, this approach offers a practical way to examine coupled biomolecular processes in complex biological systems.

REFERENCES

1. Shen, Y., Timsina, J., Heo, G., et al. (2024). CSF proteomics identifies early changes in autosomal dominant Alzheimer's disease. *Cell* **18**:6309–6326. DOI:10.1016/j.cell.2024.08.049
2. Teunissen, C.E., Verberk, I.M.W., Thijssen, E.H., et al. (2022). Blood-based biomarkers for Alzheimer's disease: towards clinical implementation. *Lancet Neurol.* **21**:66–77. DOI:10.1016/s1474-4422(21)00361-6
3. Hou, K., Ge, P., Sawaya, M.R., et al. (2025). How short peptides disassemble tau fibrils in Alzheimer's disease. *Nature* **644**:1020–1027. DOI:10.1038/s41586-025-09244-z
4. Scheltens, P., De S, B., Kivipelto, M., et al. (2021). Alzheimer's disease. *Lancet* **39**:1577–1590. DOI:10.1016/S0140-6736(20)32205-4
5. Cheng, T., Jiao, K., Sun, M.Y., et al. (2024). Internal-driven DNA nanowindmill: multi-fulcrum mediated amplified rolling nanomachine for fast and ultrasensitive electrochemical detection of tau. *Sens. Actuators B. Chem.* **423**:136797. DOI:10.1016/j.snb.2024.136797
6. Mahaman, Y.A.R., Embaye, K.S., Huang, F., et al. (2022). Biomarkers used in Alzheimer's disease diagnosis, treatment, and prevention. *Ageing Res. Rev.* **74**:101544. DOI:10.1016/j.arr.2021.101544
7. Hu, S., Zhang, L., Su, Y., et al. (2024). Sensitive detection of multiple blood biomarkers via immunomagnetic exosomal PCR for the diagnosis of Alzheimer's disease. *Sci. Adv.* 10:eabm3088. DOI: https://www.science.org/doi/10.1126/sciadv.abm3088.
8. Aron, L., Ngian, Z.K., Qiu, C., et al. (2025). Lithium deficiency and the onset of Alzheimer's disease. *Nature* **645**:712–721. DOI:10.1038/s41586-025-09335-x
9. Yang, W., Shi, Y., Zhang, Y., et al. (2024). Intranasal carrier-free nanomodulator addresses both symptomatology and etiology of Alzheimer's disease by restoring neuron plasticity and reprogramming lesion microenvironment. *ACS Nano* **18**:29779–29793. DOI:10.1021/acsnano.4c09449
10. Bao, J., Qin, M., Mahaman, Y.A.R., et al. (2018). BACE1 sumoylation increases its stability and escalates the protease activity in Alzheimer's disease. *Proc. Natl. Acad. Sci. U S A.* **115**:3954–3959. DOI:10.1073/pnas.1800498115
11. Meakin, P.J., Mezzapesa, A., Benabou, E., et al. (2018). The beta secretase BACE1 regulates the expression of insulin receptor in the liver. *Nat. Commun.* **9**:1306. DOI:10.1038/s41467-018-03755-2
12. Fotuhi, S.N., Khalaj-Kondori, M., Hoseinpour Feizi, M.A., et al. (2019). Long non-coding RNA BACE1-AS may serve as an Alzheimer's disease blood-based biomarker. *J. Mol. Neurosci.* **69**:351–359. DOI:10.1007/s12031-019-01364-2
13. Zeng, T., Ni, H., Yu, Y., et al. (2019). BACE1-AS prevents BACE1 mRNA degradation through the sequestration of BACE1-targeting miRNAs. *J. Chem. Neuroanat.* **98**:87–96. DOI:10.1016/j.jchemneu.2019.04.001
14. Lim, J., Van A, B., Koprowski, K., et al. (2025). Amplification-free, or-gated Crispr-cascade reaction for pathogen detection in blood samples. *Proc. Natl. Acad. Sci. USA.* **122**:e2420166122. DOI:10.1073/pnas.2420166122
15. Tu, T., Huan, S., Feng, X., et al. (2025). Spatial confinement of a dual activatable DNAzyme sensor in the cavity of a DNA nanocage for logic-gated molecular imaging. *Angew. Chem. Int. Ed.* **64**:e202424684. DOI:10.1002/anie.202424684
16. Yang, Q., Dong, M.J., Xu, J., et al. (2025). Crispr/RNA aptamer system activated by an and logic gate for biomarker-driven theranostics. *J. Am. Chem. Soc.* **147**:169–180. DOI:10.1021/jacs.4c08719
17. Wei, J., Wang, H., Wu, Q., et al. (2020). A smart, autocatalytic, DNAzyme biocircuit for in vivo, amplified, miRNA imaging. *Angew. Chem. Int. Ed.* **59**:5965–5971. DOI:10.1002/anie.201911712
18. Afshan, N., Cheng, T., Yu, J., et al. (2025). Catalytic hairpin assembly-based förster resonance energy transfer biosensor for simultaneous detection of multiple miRNAs from breast cancer. *Anal. Chim. Acta* **1352**:343925. DOI:10.1016/j.aca.2025.343925
19. Wang, G., Cheng, T., Yuan, H., et al. (2023). Tracing cellular interaction of circRNA-miRNA axis with cu metal-organic framework supported DNA cascade assembly. *Biosens. Bioelectron.* **228**:115226. DOI:10.1016/j.bios.2023.115226
20. Miao, P. (2023). Magnetic multipedal DNA walking nanomachine driven by catalytic hairpin assembly. *Anal. Chem.* **95**:6760–6764. DOI:10.1021/acs.analchem.3c00427
21. Meng, X., Wang, H., Yang, M., et al. (2021). Target-cell-specific bioorthogonal and endogenous ATP control of signal amplification for intracellular miRNA imaging. *Anal. Chem.* **93**:1693–1701. DOI:10.1021/acs.analchem.0c04302
22. Mao, D., Tang, X., Zhang, R., et al. (2025). Multichrome encoding-based multiplexed, spatially resolved imaging reveals single-cell RNA epigenetic modifications heterogeneity. *Nat. Commun.* **16**:958. DOI:10.1038/s41467-025-56331-w
23. Mao, D., Gou, H., Chen, W., et al. (2025). Enzymatic DNA orthogonal chemistry for multi-cancer diagnosis. *Chem* **11**:102656. DOI:10.1016/j.chempr.2025.102656
24. Wang, Y., Li, H., Cao, X., et al. (2025). In situ multiplexed imaging of miRNA heterogeneity in single urinary exosome enables non-invasive bladder cancer diagnosis. *Chem. Eng. J.* **523**:168311. DOI:10.1016/j.cej.2025.168311
25. Liu, L., Ju, P., Yang, K., et al. (2025). Extended linear confined zipper cascaded reaction for highly efficient intracellular imaging and assisting diagnosis of thyroid cancer. *Small* **21**:e2500202. DOI:10.1002/smll.202500202
26. Guo, Y., Luo, S., Liu, S., et al. (2025). Bimodal in situ analyzer for circular RNA in extracellular vesicles combined with machine learning for accurate gastric cancer detection. *Adv. Sci.* **12**:e2409202. DOI:10.1002/advs.202409202
27. Zhang, Y.P., Chen, H.J., Hu, Y., et al. (2024). Accurate cancer screening and prediction of pd-l1-guided immunotherapy efficacy using quantum dot nanosphere self-assembly and machine learning. *Nano Lett.* **24**:1816–1824. DOI:10.1021/acs.nanolett.3c05060
28. Wang, S., Zhu, Y., Zhou, Z., et al. (2024). Integrated ultrasound-enrichment and machine learning in colorimetric lateral flow assay for accurate and sensitive clinical Alzheimer's biomarker diagnosis. *Adv. Sci.* **11**:e2406196. DOI:10.1002/advs.202406196

FUNDING AND ACKNOWLEDGMENTS

The authors acknowledge the financial support from Changping laboratory (No. 2025B-07-09), National Natural Science Foundation of China (No. 82572366), and Taishan Scholars Program (tsqn202312238). The funders had no role in study design, data collection and analysis, decision to publish, or preparation of the manuscript.

AUTHOR CONTRIBUTIONS

All authors contributed to the manuscript and approved the final version.

DECLARATION OF INTERESTS

The authors declare no competing interests.